Available online at www.sciencedirect.com
ScienceDirect
Journal of Natural Gas Chemistry 19(2010)284–292
Journal of Natural Gas Chemistry
www.elsevier.com/locate/jngc

Fischer-Tropsch synthesis by nano-structured iron catalyst

Ali Nakhaei Pour[1,2*], Mohammad Reza Housaindokht[1], Sayyed Faramarz Tayyari[1], Jamshid Zarkesh[2]

1. Department of Chemistry, Ferdowsi University of Mashhad, P.O.Box 91775-1436, Mashhad, Iran;
2. Research Institute of Petroleum Industry of National Iranian Oil Company, Gas Research Division, P.O.Box 14665-137, Tehran, Iran

[Manuscript received August 24, 2009; revised September 30, 2009]

Abstract

Effects of nanoscale iron oxide particles on textural structure, reduction, carburization and catalytic behavior of precipitated iron catalyst in Fischer-Tropsch synthesis (FTS) are investigated. Nanostructured iron catalysts were prepared by microemulsion method in two series. Firstly, Fe_2O_3, CuO and La_2O_3 nanoparticles were prepared separately and were mixed to attain Fe/Cu/La nanostructured catalyst (sep-nano catalyst); Secondly nanostructured catalyst was prepared by co-precipitation in a water-in-oil microemulsion method (mix-nano catalyst). Also, conventional iron catalyst was prepared with common co-precipitation method. Structural characterizations of the catalysts were performed by TEM, XRD, H_2 and CO-TPR tests. Particle size of iron oxides for sep-nano and mix-nano catalysts, which were determined by XRD pattern (Scherrer equation) and TEM images was about 20 and 21.6 nm, respectively. Catalyst evaluation was conducted in a fixed-bed stainless steel reactor and compared with conventional iron catalyst. The results revealed that FTS reaction increased while WGS reaction and olefin/paraffin ratio decreased in nanostructured iron catalysts.

Key words

Fischer-Tropsch synthesis; iron-based catalyst; nano-particle

1. Introduction

Fischer-Tropsch synthesis (FTS) is an industrially important process for the conversion of syngas (H_2/CO) derived from carbon sources such as coal, peat, biomass, and natural gas into hydrocarbons and oxygenates [1−3]. FTS product consists of a complex multicomponent mixture of linear and branched hydrocarbons and oxygenated compounds. Fuels produced by the FTS are of a high quality due to a very low aromatic and zero sulfur content. Considerable progresses have been made in the past two decades on the development of more active and selective cobalt and iron catalysts and more effective reactor/process technologies [4,5]. Iron based catalyst systems have remained a preferred choice in commercial FTS plants due to low cost and tendency to yield high amounts of olefines in hydrocarbon distribution. But it is well known that low product selectivity, catalyst agglomeration and sintering limit use of the iron catalysts in high temperate operations [5−11]. Recent studies showed nanosized iron particles were essential to achieve high FTS activity [12−22]. The preparation method plays an important role in physical properties and performance of catalysts [16−22]. In the last years, use of microemulsion method has been developed in order to synthesize nanoparticles with controlled size and homogeneous distribution of elements [16–20]. Microemulsion system is optically transparent and has thermodynamically stable dispersion of water phase into an organic phase, which is stabilized by a surfactant [21]. If the minority phase is the aqueous one, then reversed micelles are obtained. Considering advantages such as rendering nanosized particles, displaying high surface area and low microporosity, microemulsion is an ideal technique to prepare materials containing two (or more) metallic or oxide phases [16]. In a microemulsion system, different species (oxide precursors) are homogeneously mixed within the micelles. Therefore, rendering solids display high internal homogeneity and optimal interactions between the constituents [16–20]. Some authors prepared supported iron-based Fischer-Tropsch catalysts by microemulsion method, and reported high activity and selectivity to oxygenates. However, there are still few works dealing with the preparation of non-supported catalysts even though the synthesis of mixed oxides by microemulsion has been reported [20−22].

* Corresponding author. Tel/Fax: +98 21 44739716; E-mail: nakhaeipoura@ripi.ir and nakhaeipoura@yahoo.com

doi:10.1016/S1003-9953(09)60059-1

In this work, the effects of nanoscale iron oxide particles on catalyst structure, surface area, reduction and carburization, textural properties and activity behavior of precipitated Fe/Cu/La catalyst in a fixed bed reactor, are investigated. The FTS and WGS activity, olefin selectivity and hydrocarbon product distributions are also correlated with the properties of their catalysts.

2. Experimental

2.1. Catalyst preparation

Fe/Cu/La conventional catalyst was prepared by coprecipitation of Fe and Cu nitrates at a constant pH to form porous Fe-Cu oxyhydroxide powders that were promoted by impregnation with $La(NO_3)_3$ precursor after treatment in air as described previously [23−25]. The Fe/Cu/La sep-nano catalyst was prepared by a physical mixture of prepared iron, lanthanum and copper nano-oxide [6]. The Fe/Cu/La mix-nano catalyst precursors were prepared by coprecipitation in a water-in-oil microemulsion. A water solution of metal precursors, $Fe(NO_3)_3{\cdot}9H_2O$ (Fluka, >98%) and $Cu(NO_3)_2{\cdot}4H_2O$ (Fluka, purum, >97%) was added to a mixture of an oil phase contained 1-butanol (Aldrich, >99%) and chloroform (Aldrich, >99%) with respective ratio of 60 to 40 and sodium dodecyl sulfate (SDS) as surfactant. The obtained mixture had the following composition: 10 wt% of aqueous phase, 70 wt% of oil phase and 20 wt% of surfactant. A transparent mixture, which was stable for at least 24 h, was obtained after stirring. A similar microemulsion containing NH_4OH (28.0%–30.0%) in the aqueous phase was used as the precipitating agent. Then, the mixture was set aside to decant overnight. The solid was recovered by centrifuging and was washed thoroughly with distilled water and ethanol. Finally, the sample was dried overnight at 393 K and subsequently calcined in air at 773 K for 6 h. Lanthanum promoter was added by wet impregnation method with $La(NO_3)_3$ precursor on its optimal value after treatment in air as described previously [23−25]. The promoted catalysts were dried at 383 K for 16 h and calcined at 773 K for 3 h in air. The catalyst compositions were designated in terms of atomic ratios as: 100Fe/5.64Cu/2La. All samples were pressed into pellets, crushed and sieved to obtain 100−180 μm particles.

2.2. Catalyst characterization

N_2 physisorption was carried out with surface area and pore size analyzers (Micrometertics ASAP 2010 Instruments) at 77 K to determine the BET surface area and pore size distribution of the oxide precursors. Before the measurements, the samples were degassed at 393 K for 3 h. The pore volume and the average pore diameter were calculated by Barret-Joyner-Hallender (BJH) method from the desorption isotherm. Powder X-ray diffraction (XRD) spectra of fresh catalysts were collected with a Philips PW1840 X-ray diffractometer using monochromatized Cu (K_α) radiation to determine catalyst phases after calcinations and pretreatment. For determining catalyst phases after pretreatment with syngas, the samples were passivated with an 1 vol% O_2/He mixture at room temperature for 1 h, according to a standard procedure described elsewhere [26,27]. Then the samples were analyzed by X-ray diffraction (XRD). Transmission electron microscopy (TEM) of iron nano-oxides species was determined by Philips CM 200 FEC (Field Emission Gum) transmission electron spectroscopic analyzer.

H_2-Temperature programmed reduction (H_2-TPR) profiles of the calcined catalysts were recorded by using a Micromeritics TPD-TPR 2900 system. The samples (50 mg) were heated from 350 to 1100 K at a rate of 10 K/min under flow of 5.1% hydrogen in argon gas mixture. CO-TPR was used for studying the rates of catalyst reduction and carburization using a modified method [25,28]. The samples (0.5 g) placed in a quartz cell and treated in 20% O_2 in He went through these stages: heating up to 673 K at 5 K/min, holding at 673 K for 30 min and then cooling to an ambient temperature with He. Then, the flow was switched to 20% CO in He (0.3 mol/h) and the reactor temperature was increased to 1000 K at the rate of 4 K/min. A thermal conductive detector was used to measure CO and CO_2 desorbed constantly with pulses of effluent stream, which was used to calculate the rates of oxygen removal and carbon introduction during the CO-TPR.

The H_2-TPD experiments were performed by means of the H_2 temperature programmed desorption apparatus (TPD) using 0.5 g of catalyst in a quartz reactor. The reactor was operated in a temperature range of 300 to 1100 K at a linear heating rate of 5 K/min while Ar was used as a carrier gas. A thermal conductivity detector was used to measure the H_2 desorbed in the TPD quantitatively. The catalyst was reduced with H_2 at 673 K and 0.1 MPa for 11 h. Then the sample was heated in Ar from 323 to 673 K, held at 673 K until the baseline leveled off (ensuring complete removal of adsorbed species on the reduced catalyst surface), and finally cooled to 323 K for TPD tests. In the subsequent steps, H_2 adsorption on the catalyst was performed at 323 K for 30 min, and then the sample was purged with Ar in order that weakly adsorbed species could be removed until the baseline leveled off. Following this, H_2-TPD was carried out while the temperature was increased to 1050 K. H_2 chemisorptions uptakes were determined by integrating the area of H_2-TPD curves by comparison with the known amounts of H_2 gas passed through the TCD.

The surface basicity was measured by temperature programmed desorption (TPD) of carbon dioxide (CO_2 chemisorbed at 373 K) on the reduced and purged catalyst (0.5 g) (as mentioned in H_2-TPD) packed in a shallow-bed quartz reactor with a low dead volume from 350 to 700 K at heating rate of 5 K/min with He as a carrier gas. A thermal conductivity detector was used to measure the CO_2 desorbed in the TPD quantitatively.

2.3. Catalytic performance

Catalysts were tested in a fixed-bed microreactor. A detailed description of the experimental setup and procedures has been provided elsewhere [24,25]. The catalyst samples (1.0 g catalysts diluted with 4 g quartz, 250–300 μm) were activated by a 5%(v/v) H_2/N_2 gas mixture with space velocity 15.1 nl·h^{-1}·g$_{Fe}^{-1}$ at 0.1 MPa by increasing temperature from ambient to 673 K at 5 K/min, then maintained for one hour and subsequently reduced to 543 K. The activation was followed by the synthesis gas stream with $H_2/CO = 1$ and space velocity of 3.07 nl·h^{-1}·g$_{Fe}^{-1}$ for 24 h in 0.1 MPa and 543 K before setting the FTS reaction temperature and pressure. The FTS reaction was performed at 563 K, 1.7 MPa reaction pressure, $H_2/CO = 1$ and space velocity of 4.9 nl·h^{-1}·g$_{Fe}^{-1}$.

The products were analyzed by means of three gas chromatographs, a Shimadzu 4C gas chromatograph equipped with two sequentially connected packed columns: Porapak Q and Molecular Sieve 5A, and a thermal conductivity detector (TCD) with argon which was used as a carrier gas for hydrogen analysis. A Varian CP 3800 with a chromosorb column and a thermal conductivity detector (TCD) were used for CO, CO_2, CH_4, and other non-condensable gases, and a Varian CP 3800 with a Petrocol^{Tm} DH100 fused silica capillary column and a flame ionization detector (FID) were used for organic liquid products so that a complete product distribution could be provided.

3. Results and discussion

3.1. Textural structure of the catalysts

BET surface area, pore volume and pore diameter of the catalysts are summarized in Table 1. The BET surface areas of the oxide precursors are in the range of 22–45 m^2/g. By comparing the BET surface areas of the catalysts prepared by different preparation methods, the catalysts prepared by microemulsion method have higher BET surface area than conventional catalyst. Regarding two nanostructured catalysts, the sep-nano catalyst has higher surface area than mix-nano catalyst. Because Fe/Cu/La precursors were calcined again after the impregnation of La containing solution, it is reasonable to assume that the re-calcinations after the impregnation cause the sintering of Fe_2O_3 particles in these precursors. The pore volume of these oxide precursors decreases in a similar order to that observed for the surface area. The sep-nano catalyst has the largest pore volume, whereas conventional catalyst has the smallest one. The average pore diameter of these precursors shows an opposite trend.

Table 1. N_2 adsorption at 77 K and H_2 uptake on reduced catalysts

Catalysts	BET surface area (m^2/g)	Pore volume[a] (cm^3/g)	Average pore diameter[a] (nm)	H_2 uptake[b] ($\times10^{-2}$ mmol H_2/mmol Fe)
Conventional	22	0.15	21.6	8.3
Sep-nano	45	0.32	14.1	9.8
Mix-nano	43	0.31	14.6	10.1

[a]These values were calculated by BHJ method from desorption isotherm;
[b]The H_2 uptake on catalysts was determined by calculating the area under the H_2-TPD curves, until H_2 disappeared in effluent of reactor

3.2. Temperature programmed desorption (TPD) of catalysts

The catalyst TPD studies were performed by hydrogen and carbon dioxide in order to determine adsorption properties of catalysts. Table 1 shows the H_2 chemisorption uptakes of the catalysts. As shown in Table 1, the H_2 adsorption increased from 8.4 to 10.1 $\times10^{-2}$ mmol H_2/mmol Fe while the catalyst crystal size decreased from conventional to mix-nano-catalyst.

Figure 1 shows the H_2 uptake on catalysts vs. the temperature. It displays that H_2 desorption takes place on two kinds of catalytic sites. The low temperature peak is attributed to the catalytic sites that are affected by Cu promoter. In contrast, the high temperature peak indicates the catalytic sites that are not affected by Cu [25]. As shown in this Figure and Table 1, the H_2 adsorption uptake improves by decreasing the catalyst crystal size from conventional to nano-particles. Also, the first peak is smaller and the second peak is bigger for sep-nano-catalyst in comparison with the mix-nano catalyst. It contributes to separate production of nano-particles of iron and copper oxides in nano-catalyst that decreases the cooperation of copper and iron oxides.

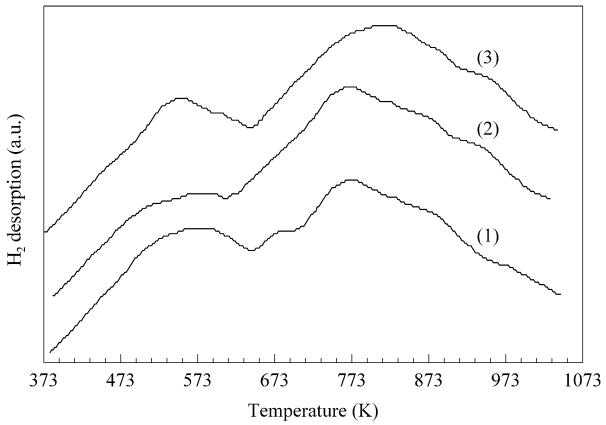

Figure 1. H_2-TPD on reduced catalysts. (1) Fe/Cu/La conventional catalyst, (2) Fe/Cu/La sep-nano catalyst, (3) Fe/Cu/La mix-nano catalyst

Carbon dioxide uptakes are often used as a probe to determine the intensity and strength of the surface basicity sites in solid materials [29]. The CO_2 -TPD curves of the catalysts are shown in Figure 2. As shown in this Figure, there are several peaks in the TPD profiles. A small peak at about 373 K and a long tail at a temperature above 620 K can be traced in all profiles. The small peak at a low temperature corresponds to weak CO_2 physical adsorption in the bulk phase. The peak tail above 620 K is due to the slow decomposition of metal carbonates formed during CO_2 adsorption [30]. In the temperature range 373–600 K, there are two clear peaks

caused by desorption of CO_2 that interact moderately with the surface basic sites. The CO_2-TPD results show that the carbon dioxide desorption in conventional and mix-nano catalysts was higher than sep-nano-catalyst. While the amount of La_2O_3 for all catalysts is equal, La was impregnated on the surface after co-precipitation of Fe and Cu in conventional and mix-nano catalysts. Therefore, it caused to have more concentration of La on the surface of these catalysts.

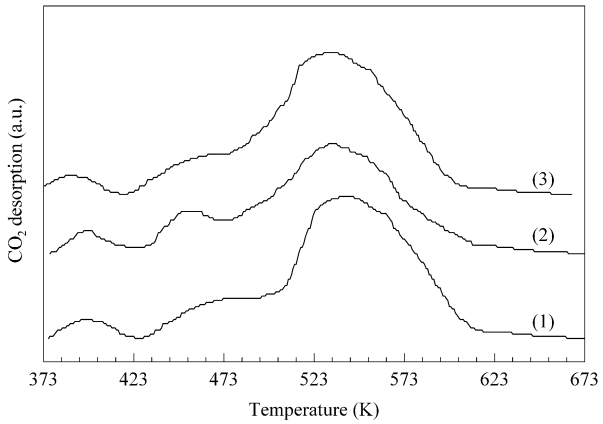

Figure 2. CO_2-TPD on reduced catalysts. (1) Fe/Cu/La conventional catalyst, (2) Fe/Cu/La sep-nano catalyst, (3) Fe/Cu/La mix-nano catalyst

3.3. Reduction and carburization of the catalysts

H_2-Temperature programmed reduction (H_2-TPR) measures the effects of catalyst crystal size and preparation method on the reduction mechanism of the catalysts. TPR pattern of conventional and nanostructured catalysts are shown in Figure 3. TPR patterns of conventional and mix-nano iron catalysts present two main reduction peaks at about 600 and 950 K in H_2-TPR profile. It has been postulated that the first stage corresponds to the reductions of Fe_2O_3 to Fe_3O_4 and CuO to Cu. The second stage corresponds to subsequent reductions of Fe_3O_4 to metallic iron [31]. The presence of Cu in iron catalyst reduces Fe_2O_3 to Fe_3O_4 at lower temperature rather than Cu-free samples [1−5]. As CuO reduces, Cu crystallites nucleate and provide H_2 dissociation sites, which in turn lead to reactive hydrogen species capable of reducing iron oxides at relatively low temperatures [16,25,28]. Better interaction between iron and copper oxides in homogeneous phase of mix-nano catalyst caused to shift the first reduction peak to lower temperature in H_2-TPR in comparison with other catalysts. Smaller crystal size in nano-catalyst has weak influence on the reduction of Fe_3O_4 to Fe, because thermodynamics and the nucleation of new crystal structures control the reduction rates at higher temperatures instead of H_2 dissociation steps [28]. Comparison of H_2 consumed in reduced process shows that amount of catalyst reduction increased with decreasing the catalyst crystal size from conventional catalyst to nano size. TPR pattern of sep-nano size iron catalyst presents three main reduction peaks at about 500, 650 and 950 K. In this catalyst the reduction of Fe_2O_3 to Fe_3O_4 and CuO to Cu occurred separately. Consequently, it is concluded that the first and second peaks correspond to the reduction of CuO to Cu and Fe_2O_3 to Fe_3O_4, respectively. As explained in pervious section, the separated reduction of CuO to Cu and Fe_2O_3 to Fe_3O_4 are attributed to segregate production of nano-particles of iron and copper oxides in sep-nano catalyst that decreased the cooperation of copper and iron oxides in this method for production of sep-nano catalyst in comparison with mix-nano and conventional catalysts (both iron and copper were co-precipitated together). The Fe_2O_3 reduction to Fe_3O_4 shifts to a higher temperature with the cooperation of the copper and iron oxides in sep-nano catalyst decreases. The third stage corresponds to subsequent reduction of Fe_3O_4 to metallic iron.

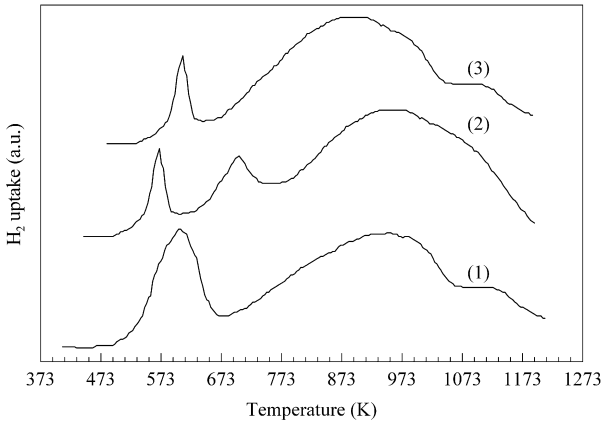

Figure 3. H_2-TPR of the catalysts. (1) Fe/Cu/La conventional catalyst, (2) Fe/Cu/La sep-nano catalyst, (3) Fe/Cu/La mix-nano catalyst

Quantitative results of hydrogen consumption are shown in Table 2. Assuming that the first peak area in H_2-TPR profile corresponds to the reduction of Fe_2O_3 to Fe_3O_4 and CuO to Cu (for sep-nano catalyst, consider the first two peaks together) and the second peak area corresponds to the reduction of Fe_3O_4 to Fe, concludes the experimental value of the peak area ratio (Table 2). Compared to the theoretical calculations, the experimental value was small. These results suggest that a small amount of Fe_2O_3 was reduced to metallic iron and similar to those previous studies of supported iron catalysts [32,33]. It is concluded that the amount of catalyst reduction is increased by reducing the catalyst particle size.

Table 2. Quantitative TPR results

Catalyst	Peak area ratio		Catalyst reduction
	theoretical	experimental	(mol%)
Conventional	6.7	4.1	61.2
Sep-nano	6.7	4.9	73.1
Mix-nano	6.7	5.3	79.1

The effects of crystal size on CO-TPR of catalysts are shown in Figure 4. The CO-TPR study of catalysts is divided into two parts: Oxygen removal from catalyst lattice and carbon introduction into the catalyst lattice. Two general stoichiometric reactions are involved in the carburization of Fe oxides [25,28]. The removal of lattice oxygen occurs via:

$$Fe_xO + CO \longleftrightarrow Fe_x + CO_2 \quad (1)$$

Initially, Fe oxides are reduced to form CO_2 and Fe center with lower valence than Fe_2O_3; in the next sequential or alternate step, CO carburizes Fe oxides to form CO_2 and Fe carbides:

$$Fe_x + 2CO \longleftrightarrow Fe_xC + CO_2 \quad (2)$$

In this step, oxygen removal and carbon deposition occur concurrently. The excess amount of consumed CO in comparison with that to produce CO_2 provides a certain amount of the carbon that has been retained by the sample. The different CO and CO_2 stoichiometries associated with these two steps allow the net rates of oxygen removal and carbon deposition steps to be decoupled by using the following equations:

$$R_O = \text{Oxygen removal rate} = 2R_{CO_2} - R_{CO} \quad (3)$$

$$R_C = \text{Carbon introduction rate} = R_{CO} - R_{CO_2} \quad (4)$$

where, R_{CO_2} is rate of CO_2 formation and R_{CO} is the rate of CO consumption. As shown in Figure 4, the individual rates of oxygen removal and the carbon introduced by CO, which are largely a function of temperature, can be calculated by monitoring the concentration of CO and CO_2 in the effluent stream. The first peak in the oxygen removal pattern of the catalysts is recognized as a reduction of the solid solution for CuO to Cu and Fe_2O_3 to Fe_3O_4, and the second peak is attributed to the reduction and carburization of Fe_3O_4 species into FeC_x [25,28,30]. In sep-nano catalyst, the first peak is divided in two parts that shows the reduction of CuO and Fe_2O_3 is occurred separately, same as explained in H_2-TPR section. All of the removable oxygen in the catalyst lattice was eliminated and the excess CO introduced into the catalyst was used to enhance transformation among the various iron carbides while the carbon introduction rate increased. As shown in Figure 4, the oxygen removal increased due to better interaction of oxygen lattice with CO as a carrier of oxygen when the crystal size of catalyst decreased. However, a faster nucleation of FeC_x crystallites on nano-scale surface oxides shifts the second peak (oxygen removal pattern) to lower temperature in nano catalysts. According to the pattern of the carbon introduction, the first peak corresponds to the Fe_3O_4 transformation to iron carbide. It is found that the peak over the 600 K increased in nano-catalyst. This difference strongly suggests that the decrease in catalyst crystal size enhances the carburization of iron particles, which produces more carbon rich iron carbides ($\acute{\varepsilon}$-carbide $Fe_{2.2}C$) and can lead to a significant carbon deposition with syngas during the reduction period [12,34]. Above 725 K, CO disproportion occurs via the Boudouard reaction with the formation of excess amorphous carbon [25,28,30]. Xu and Bartholomew [35] have identified six different carbonaceous species in the iron-based catalysts. They suggested a series of transformation of C_α (atomic carbonaceous species, and lightly polymerized surface carbon species formed by CO dissociation on the catalyst surface) to $\acute{\varepsilon}$-$Fe_{2.2}C$ carbide and then to Hägg carbide (χ-$Fe_{2.5}C$). As shown in Figure 4, increase in the carbon deposition ability on the nanostructured iron catalyst affects the catalyst activity and also increases the catalyst deactivation rate by covering the active sites of the catalyst with coke deposition during the FTS reaction.

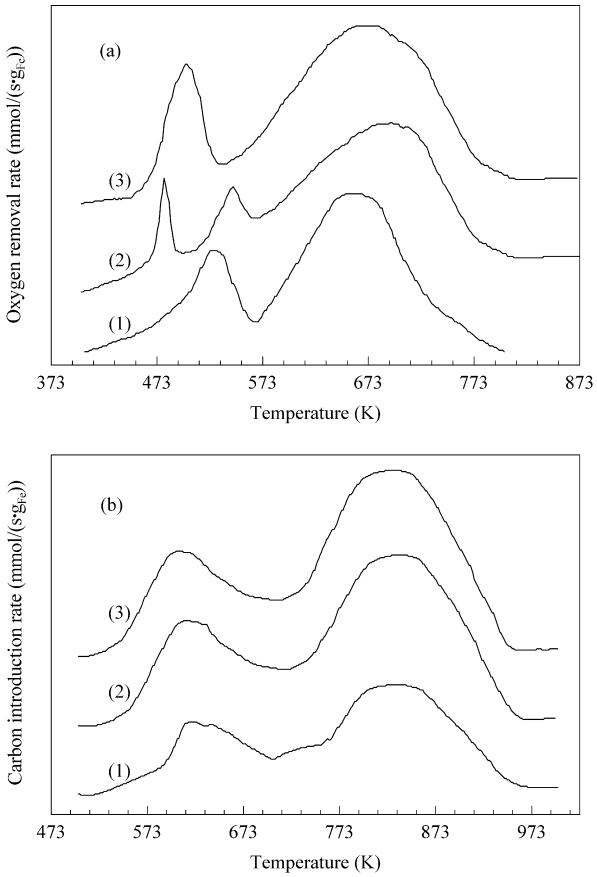

Figure 4. Oxygen removal and carbon introduction rates for the catalysts in CO. (1) Fe/Cu/La conventional catalyst, (2) Fe/Cu/La sep-nano catalyst, (3) Fe/Cu/La mix-nano catalyst

3.4. Crystalline structures in catalysts

Nanostructure and conventional iron catalysts were studied by XRD measurements after calcinations. The results are displayed in Figure 5. The pattern of all the catalysts indicates that rhombohedral hematite (Fe_2O_3) with corundum-type structure has characteristic diffraction peaks at 2θ values of 24.3°, 33.3°, 35.8°, 40.8°, 49.6°, 54.1°, 57.6° and 64.1° [28,31]. The average size of the crystal size of the conventional, sep- and mix-nano catalysts were determined to be about 42, 20 and 22 nm by using Scherrer equation, respectively. Diffraction data for these catalysts indicate that the presence of lanthanum and copper and subsequent treatment in dried air did not influence the hematite crystalline phases detected by X-ray diffractions in these different methods of catalyst preparations. It shows that the hematite structure once formed remained stable during subsequent aqueous impregnation and thermal treatment.

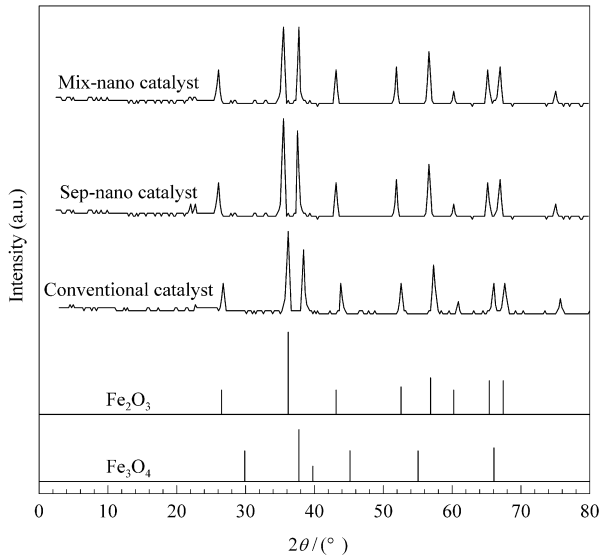

Figure 5. X-Ray diffraction patterns of calcined catalysts

XRD analysis of the passivated pretreated samples is depicted in Figure 6. A summary of the nature of the different species detected from the XRD analysis (according to the JCPDS card) after the pretreatments is shown in Table 3. As shown in Figure 6 and Table 3, iron carbide phases are formed under syngas pretreatment. As the reduction of the catalyst proceeded, iron oxide was transformed from $Fe_2O_3 \rightarrow Fe_3O_4 \rightarrow \alpha$-Fe or iron carbide. α-Fe could not be observed in our reduced catalyst because the metallic iron was fairly reactive to carbon dissociated from carbon monoxide. Among the iron carbides, O carbides (carbides with carbon atoms in octahedral interstices, ε-Fe_2C and ε-$Fe_{2.2}C$) and TP carbides (carbides with carbon atoms in trigonal prismatic interstices, χ-$Fe_{2.5}C$ and θ-Fe_3C) have been identified [26]. According to the JCPDS card, only $\acute{\varepsilon}$-$Fe_{2.2}C$ shows a main diffraction peak near 43° among these carbides [36]. Furthermore, peaks at ca. 39° and 41° can be used for identification of Hägg carbide (χ-$Fe_{2.5}C$) (JCPDS 36−1248). Peak assignation was based on the characteristic angles of cementite carbide (θ-Fe_3C) (JCPDS 76−1877) at 78.0° and 70.1°, which are not present in the diffractogram of the sample χ-$Fe_{2.5}C$ [26]. On the other hand, sharp peaks are clearly observed at 35°, 57° and 63° as well in the diffraction profiles which are assigned to Fe_3O_4. The assignment of the different Fe carbide phases ($\acute{\varepsilon}$-$Fe_{2.2}C$, θ-Fe_3C and χ-$Fe_{2.5}C$) from the X-ray diffractograms must be performed carefully because they show similar diffraction patterns. The relative intensity of the diffraction peaks was also taken into account for the correct identification of the carbide species. As shown in Figure 6 and Table 3, the nano-catalysts have greater amount of carbon-rich $\acute{\varepsilon}$-carbides than conventional catalyst, which has more iron-rich χ and θ phases instead. These results contribute to lower size of iron crystals in nano-catalysts that increased the contact chances between carbon monoxide and the bulk iron in pretreatments of catalysts with syngas and converted more bulk iron to carbon — rich $\acute{\varepsilon}$-$Fe_{2.2}C$ carbides. Raupp and Delgass [37] concluded that the bulk iron acts as a getter for carbon and leads to control the surface composition in pretreatment and FTS reaction. Previous results suggest that the most catalytic active phase in FTS is $\acute{\varepsilon}$-carbide ($Fe_{2.2}C$), which over long periods of reaction is converted into the Hägg carbide (χ-$Fe_{2.5}C$) and subsequently converts into the cementite (θ-Fe_3C) with lower carbon content [26,38].

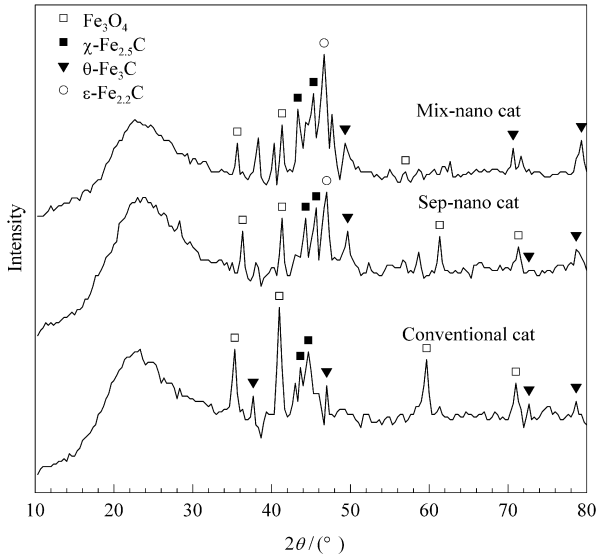

Figure 6. X-Ray diffraction patterns of catalysts after activation pretreatments (H_2/CO at 673 K for 24 h)

Table 3. Phase detected by XRD after activation pretreatment with syngas

Catalyst	Phases detected	Fe-carbides/Fe_3O_4 ratio	$\acute{\varepsilon}$-$Fe_{2.2}C$/(θ-Fe_3C, χ-$Fe_{2.5}C$) ratio
Conventional	Fe_3O_4, θ-Fe_3C, χ-$Fe_{2.5}C$	1.6	0.7
Sep-nano	Fe_3O_4, θ-Fe_3C, χ-$Fe_{2.5}C$, $\acute{\varepsilon}$-$Fe_{2.2}C$	2.7	1.6
Mix-nano	Fe_3O_4, θ-Fe_3C, χ-$Fe_{2.5}C$, $\acute{\varepsilon}$-$Fe_{2.2}C$	3.8	2.2

χ-$Fe_{2.5}C$: Hägg carbide, θ-Fe_3C: cementite carbide, Fe_3O_4: magnetite

The TEM micrographs for all oxides are shown in Figure 7. As shown in these Figures, the crystal size of the sep and mixed-nano catalysts were determined to be 20 and 21.6 nm, respectively. Similar results were obtained by using the XRD results and Scherrer equation.

3.5. Catalyst activity

The samples were tested in the FTS reaction at 563 K for 250 h. The CO conversions versus time-on-stream plots for samples are depicted in Figure 8. The CO conversion im-

proved significantly while the catalyst crystal size decreased. The chemical composition of the sample played a key role on its catalytic performance. As mentioned in previous section, the main iron carbide produced in nano catalysts is $\acute{\varepsilon}$-carbide ($Fe_{2.2}C$). Pervious results suggest that the $\acute{\varepsilon}$-carbide ($Fe_{2.2}C$), which is produced in higher amounts than Hägg carbide (χ-$Fe_{2.5}C$) and cementite (θ-Fe_3C) in iron nano-particles after pretreatment, is the most catalytically active phase in FTS reaction. The higher activity of nano catalysts contributes to this fact. The mix-nano iron catalyst has higher FTS activity due to superior reduction amounts in pretreatment. Also, reduction amounts and ability of the H_2 adsorption of the catalyst, which improved with decreasing in crystal size of the catalyst, caused to higher activity of nano scale of iron particles.

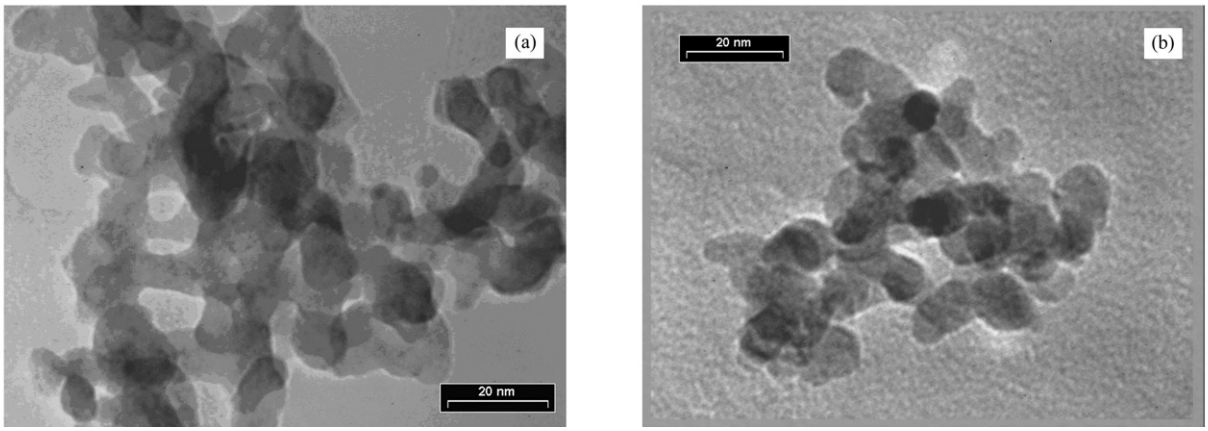

Figure 7. TEM images of the (a) mixed-nano, (b) sep-nano catalysts

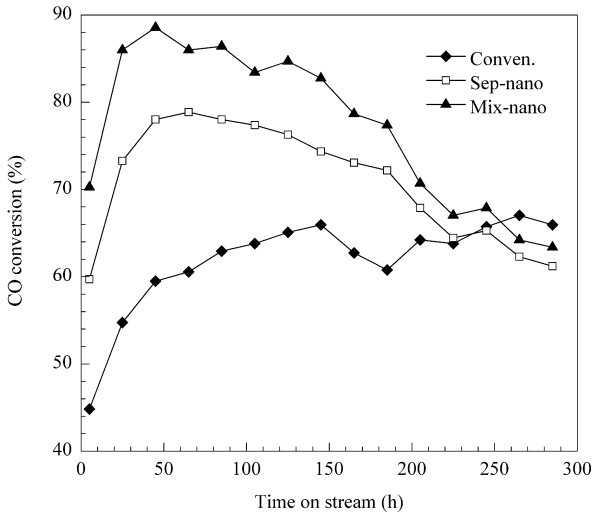

Figure 8. Variation of CO conversion as a function of time-on-stream. Reaction conditions: 563K, $H_2/CO = 1$, 1.7 MPa, SV = 4.9 $nl \cdot h^{-1} \cdot g_{Fe}^{-1}$

As shown in Figure 8, the nanostructured catalysts have higher catalyst deactivation rate and the CO conversion drops rapidly in comparison with conventional catalysts. Eliason and Bartholomew [39] provided evidences that sintering was not responsible for activity loss in iron catalyst. Jung and Thomson [40] speculated that carbon atoms precipitated by the $\acute{\varepsilon}$ to χ transformation serve nucleation sites for Boudouard reaction. Eliason and Bartholomew [41] assumed the formed carbon atoms in carbide transformations serve nucleation sites for polymerization to β-carbon and/or crystallization to graphitic δ-carbon. Therefore, in this work, observed loss of activity is attributed to the transformation of the active carbons into inactive carbons and active carbides into lower active carbides.

Since $\acute{\varepsilon}$-carbide ($Fe_{2.2}C$) phase is the most active type among the iron carbide in FTS synthesis, converting this active phase ($\acute{\varepsilon}$-carbide) into the Hägg carbide (χ-$Fe_{2.5}C$) with lower FTS activity and subsequently into the cementite (θ-Fe_3C) with lower carbon content cause to decrease in FTS reaction activity quickly in nanostructured catalysts. Catalyst deactivation process is very complicated and it is not the subject of this study.

Table 4 shows the effect of the catalyst crystal size on catalyst activity, product selectivity and hydrocarbons distribution with different space velocity at the same time-on stream. The methane selectivity increased and the CO_2 selectivity decreased at the same time on stream from conventional to nano catalyst. Selectivity toward higher hydrocarbons shows drop off trend in carbon number from conventional to nano catalyst.

The H_2-TPD and CO_2-TPD results show that the low-sized catalyst crystal improves H_2 and decreases CO concentrations on the surface of the catalysts. Higher H_2 and lower CO concentrations on nanostructured catalyst surface prevent chain growth reaction, decrease selectivity to higher hydrocarbons and enhance the hydrogenation of olefin, in comparison with conventional catalyst. The results presented in Table 4 show that the olefin/paraffin ratios are decreased from conventional to nano-catalysts. It is well known that 1-alkenes are primary products of the FTS reaction over iron-based catalyst and they react further to paraffin by hydrogenation as a secondary reaction [1−5]. The olefin/paraffin ratio is a basis ratio to demonstrate the presence of the secondary reactions in total FT synthesis [1−5]. Hydrogenation of 1-alkenes to paraffin is the most famous secondary reaction in FT synthesis. Because of higher concentration of hydrogen on surface of nanostructured iron particles, the formation of paraffin via hydrogenation of 1-alkenes improves.

Table 4. Activity and products selectivity of catalysts after 105 h

Catalyst	X^{a}_{CO}	HC[b]	O/P[c]	α[d]	CO_2 (%)[e]	Product selectivity			
						CH_4	C_2–C_4	C_5–C_{12}	C_{12+}
Conventional	64.1	24.5	1.3	0.65	36.3	16.6	35.2	29.4	18.8
Sep-nano	77.2	29.2	1.0	0.59	32.2	19.1	37.8	32.3	10.8
Mix-nano	83.3	31.1	1.1	0.61	31.1	18.3	36.6	31.9	13.2

Reaction conditions: 563 K, 1.7 MPa, $H_2/CO = 1$, space velocity = 4.9 $nl \cdot h^{-1} \cdot g_{Fe}^{-1}$;
[a]Carbon monoxide conversion (mol%);
[b]Hydrocarbon production, $gCH_2/gFe/s$ ($\times 10^5$), CH_4 free;
[c]Olefin to paraffin ratio;
[d]Chain growth probability;
[e]CO_2 selectivity. Selectivity to oxygenates was negligible ($< 2.0\%$) in all cases

The selectivity toward carbon dioxide was higher for conventional catalyst due to their higher activity in the water-gas shift reaction. It is generally accepted that the FTS and water-gas-shift (WGS) reactions engage on different active sites over a precipitated iron catalyst. Literature suggests that the formation of iron carbides result in high FTS activity and the magnetite (Fe_3O_4) is the most active phase for WGS reaction [5]. H_2-TPR results show that the amount of magnetite (Fe_3O_4) phase in conventional catalyst is higher than others. Therefore, conventional catalyst has higher activity for water-gas shift reaction.

4. Conclusions

In this study, nanostructured catalysts were prepared in two series. Firstly, Fe_2O_3, CuO and La_2O_3 nanoparticles were prepared separately by microemulsion method and then mixed together. In another method iron and Cu oxides were prepared by coprecipitation microemulsion method. Catalyst evaluation was conducted in a fixed-bed stainless steel reactor and compared with conventional iron catalyst. It was found that the catalytic activity in FTS reaction was increased with decreasing the crystal size of the catalyst from conventional to nano catalysts. These results contribute higher amount of $\acute{\varepsilon}$-carbide ($Fe_{2.2}C$) rather than Hägg carbide (χ-$Fe_{2.5}C$) and cementite (θ-Fe_3C) in iron nano-particles after pretreatment in nanostructured iron catalysts. The olefin/paraffin ratios are decreased from conventional to nano-catalysts because of higher H_2 and lower CO concentration on nano-catalyst surface than conventional catalyst.

References

[1] Anderson R B. The Fischer-Tropsch Synthesis. Orlando: Academic Press, 1984
[2] Dry M E. In: Anderson J R, Boudart M eds. Catalysis-Science and Technology. New York: Springer-Verlag, 1981. 159
[3] Bartholomew C H. Recent Developments in Fischer-Tropsch Catalysis, New Trends in CO Activation, Studies in Surface Science and Catalysis. Amsterdam: Elsevier, 1991.
[4] Kölbel H, Ralek M. *Catal Rev Sci Eng*, 1980, 21: 225
[5] van der Laan G P, Beenackers A A C M. *Catal Rev Sci Eng*, 1999, 41: 255
[6] Pour A N, Shahri S M K, Zamani Y, Irani M, Tehrani S. *J Natur Gas Chem*, 2008, 17: 242
[7] Pour AN, Shahri SMK, Zamani Y, Zamanian A. *J Natur Gas Chem*, 2010, 19:193
[8] Pour AN, Zare M, Shahri SMK, Zamani Y, Alaei MR. *J Natur Gas Sci Eng*, 2009, 1:183
[9] Pour AN, Zare M, Zamani Y. *J Natur Gas Chem*, 2010, 19:31
[10] Schulz H. *Appl Catal A*, 1999, 186: 3
[11] Dry M E. *Catal Today*, 2002, 71: 227
[12] Sarkar A, Seth D, Dozier A K, Neathery J K, Hamdeh H H, Davis B H. *Catal Lett*, 2007, 117: 1
[13] Pour A N, Taghipoor S, Shekarriz M, Shahri S M K, Zamani Y. *J Nanosci Nanotech*, 2009, 9: 4425
[14] Hayashi H, Chen L Z, Tago T, Kishida M, Wakabayashi K. *Appl Catal A*, 2002, 231: 81
[15] Li X, Zhong B, Peng S, Wang Q. *Catal Lett*, 1994, 23: 245
[16] Herranz T, Rojas S, Perez-Alonso F J, Ojeda M, Terreros P, Fierro J L G. *Appl Catal A*, 2006, 311: 66
[17] Pour AN, Housaindokht MR, Faramarz ST, Zarkesh J, Alaei MR. *J Natur Gas Sci Eng*, 2010, in press, doi:10.1016/j.jngse.2010.02.004
[18] Pour AN, Housaindokht MR, Faramarz ST, Zarkesh J. *J Natur Gas Sci Eng*, 2010, in press, doi:10.1016/j.jngse.2010.04.001
[19] Pour AN, Housaindokht MR, Faramarz ST, Zarkesh J. *J Natur Gas Chem*, 2010 19:107-116
[20] Eriksson S, Nylen U, Rojas S, Boutonnet M. *Appl Catal A*, 2004, 265: 207
[21] Schwuger M J, Stickdorn K, Schomaecker R. *Chem Rev*, 1995, 95: 849
[22] Liu C, Zou B, Rondinone A J, Zhang Z J. *J Phys Chem B*, 2000, 104: 1141
[23] Pour A N, Zamani Y, Jozani K J, Mehr J Y. EP 1 657 290. 2006
[24] Pour A N, Zamani Y, Tavasoli A, Shahri S M K, Taheri S A. *Fuel*, 2008, 87: 2004
[25] Pour A N, Shahri S M K, Bozorgzadeh H R, Zamani Y, Tavasoli A, Marvast M A. *Appl Catal A*, 2008, 348: 201
[26] Herranz T, Rojas S, Perez-Alonso F J, Ojeda M, Terreros P, Fierro J L G. *J Catal*, 2006, 243: 199
[27] Shroff M D, Datye A K. *Catal Lett*, 1996, 37: 101
[28] Li S, Li A, Krishnamorrthy S, Iglesia E. *Catal Lett*, 2001, 77: 197
[29] Bouarab R, Cherifi O, Auroux A. *Thermochim Acta*, 2005, 434: 69
[30] Yang J, Sun Y, Tang Y, Liu Y, Wang H, Tian L, Wang H, Zhang Z, Xiang H, Li Y. *J Mol Catal A*: *Chem*, 2006, 245: 26
[31] Raje A P, O'Brien R J, Davis B H. *J Catal*, 1998, 180: 36
[32] Bukur D B, Sivaraj C. *Appl Catal A*, 2002, 231: 201
[33] Hayakawa H, Tanaka H, Fujimoto K. *Appl Catal A*, 2006, 310: 24

[34] Davis B H. (1999) Technology development for iron Fischer-Tropsch Catalysis, US DOE Final Technical Report, Contract # DE-AC22-94PC94055-13
[35] Xu J, Bartholomew C H. *J Phys Chem B*, 2005, 109: 2392
[36] Ning W, Koizumi N, Chang H, Mochizuki T, Itoh T, Yamada M. *Appl Catal A*, 2006, 312: 35
[37] Raupp G B, Delgass W N. *J Catal*, 1979, 58: 361
[38] Amelse J A, Butt J B, Schwartz L H. *J Phys Chem*, 1978, 82: 558
[39] Eliason S A, Bartholomew C H. In: Bartholomew C H, Butt J B eds. Catalyst Deactivation. Amsterdam: Elsevier, 1991. 211
[40] Jung H, Thomson W J. *J Catal*, 1992, 134: 654
[41] Eliason S A, Bartholomew C H. *Appl Catal A*, 1999, 186: 229